Chinese Journal of
POLYMER SCIENCE

RESEARCH ARTICLE

https://doi.org/10.1007/s10118-026-3780-9
Chinese J. Polym. Sci.

Synergistic Spring-entanglement Network Design of High-modulus and Low-hysteresis Ionic Elastomers for High-fidelity Sensing

Ting Cui[a], Jing-Ming Cai[c,d], Cun-Yi Li[e], Zhou-Yue Lei[a,b*], and Pei-Yi Wu[a*]

[a] *State Key Laboratory of Advanced Fiber Materials, College of Chemistry and Chemical Engineering, Center for Advanced Low-Dimension Materials, Donghua University, Shanghai 201620, China*
[b] *State Key Laboratory of Digital Medical Engineering, School of Biological Science and Medical Engineering, Southeast University, Nanjing 210096, China*
[c] *School of Civil Engineering, Southeast University, Nanjing 210000, China*
[d] *School of Mechanical and Mechatronic Engineering, University of Technology Sydney, 817 Broadway, Ultimo, NSW, 2007, Australia*
[e] *Department of Civil Engineering, Aalto University, Espoo 02150, Finland*

Electronic Supplementary Information

Abstract The development of high-performance ionotronics is currently hindered by the fundamental trade-off between mechanical robustness (high modulus and toughness) and functional reliability (low hysteresis and high elasticity). Conventional toughening mechanisms that rely on sacrificial bonds inevitably introduce significant energy dissipation and irreversible creep, leading to fatal signal drifts in long-term applications. Herein, we report a synergistic spring-entanglement network that achieves simultaneous optimization of the modulus, recovery, and extensibility *via* topological modulation. By utilizing a click-chemistry-derived covalent framework as a stiff athermal spring, the elastomer achieved a skin-like modulus (approximately 1 MPa) and near-zero hysteresis (<0.51%). The strategic integration of ultra-high-molecular-weight polymer entanglements introduces topological constraints that function as non-dissipative stress delocalisers, facilitating a fracture strain of 142% without compromising the instantaneous restorative force. This architecture maintains low hysteresis and high elasticity over 10000 cycles, ensuring impeccable signal fidelity and negligible baseline drift in multimodal sensing. This synergistic topological design provides a robust foundation for reliably stable human-machine interfaces and precision ionotronics.

Keywords Elastomers; Ionotronics; High elasticity; Sensing; High-fidelity

Citation: Cui, T.; Cai, J. M.; Li, C. Y.; Lei, Z. Y.; Wu, P. Y. Synergistic spring-entanglement network design of high-modulus and low-hysteresis ionic elastomers for high-fidelity sensing. *Chinese J. Polym. Sci.* https://doi.org/10.1007/s10118-026-3780-9

INTRODUCTION

Biological tissues possess a finely tuned synergy of modulus, extensibility, and elasticity, enabling them to sustain dynamic deformation with minimal energy loss. Emulating this balance is crucial for next-generation ionotronics, including human-machine interfaces, soft robotics, and wearable electronics, where mechanical compliance, durability, and signal fidelity are simultaneously required.[1–3] Among the emerging candidates, ion-conductive elastomers are particularly promising owing to their intrinsic softness and ionic conductivity. However, the development of these materials is currently hindered by a fundamental trilemma: the mutual exclusivity of high elastic modulus, large stretchability, and ultra-low hysteresis, which stems from the intrinsic thermodynamic trade-off between segmental relaxation dynamics and cohesive interaction density.[4,5]

In a single-network architecture, the elastic modulus is typically enhanced by increasing cross-linking density. However, according to the Lake-Thomas model, the energy required to fracture a polymer network is proportional to the number of bonds per unit volume that must be stretched to their limit, and an increase in cross-linking density severely reduces the length of polymer chains between junctions, leading to a precipitous decline in both extensibility and fracture energy.[6,7] To bypass this limitation, double-network (DN) strategies have been developed, employing a rigid sacrificial network to provide the initial strength and a flexible network to sustain large deformations.[8] Although effective in elevating the toughness, the mechanical performance of DN systems is fundamentally predicated on the irreversible rupture of sacrificial bonds. This energy-dissipative process inevitably induces substantial mechanical hysteresis and hinders the rapid elastic recovery.[9,10] Such sacrificial mechanisms cause structural fatigue and cumulative signal baseline drift under cyclic loading, thereby compromising the reliability of soft electronics. Fundamentally, these limitations originate from the stochastic and heterogeneous topology of conventional polymer networks, where the uncontrolled spatial distribution of

* Corresponding authors, E-mail: leizhouyue@seu.edu.cn (Z.Y.L.)
E-mail: wupeiyi@dhu.edu.cn (P.Y.W.)
Invited Research Article
Received May 11, 2026; Accepted June 10, 2026; Published online August 19, 2026

cross-links prevents precise engineering of an ideal elastic energy landscape.[11,12] This randomness makes it nearly impossible to achieve stiffness in the megapascal regime without sacrificing the entropy-driven recovery required for high-frequency sensing.

To overcome these long-standing trade-offs, we introduce a synergistic spring-entanglement network that independently modulates the elastic and dissipative responses *via* topological engineering. By utilizing a high-efficiency thiol-ene click reaction, we designed a homogeneous covalent scaffold that functions as an athermal molecular spring, ensuring a high skin-like modulus (approximately 1 MPa) and near-zero hysteresis (<0.51%). Simultaneously, we integrated high-molecular-weight polymer chains to form topologically entangled domains. These domains function as non-dissipative stress distributors that alleviate stress concentration *via* controlled segmental sliding, while their slower relaxation ensures that they do not interfere with the instantaneous restorative force of the covalent network. This architecture confers high elasticity through an ideal spring network, whereas the incorporation of entanglement regions reconciles the competing demands of load bearing and stress redistribution. Consequently, the synergistic spring-entanglement ionic elastomer (S-SEIE) maintained mechanical stability over 10^4 cycles, providing an approach for fatigue-resistant, high-fidelity bio-integrated devices.

EXPERIMENTAL

The detailed experimental section can be found in the electronic supplementary information (ESI).

RESULTS AND DISCUSSION

Design, Synthesis, and Architecture of the S-SEIE

Achieving simultaneous optimization of modulus, stretchability, and elasticity in soft ionotronics remains a longstanding challenge, primarily because of the intrinsic structural and dynamic coupling in conventional polymer networks. Stochastic free-radical polymerization typically yields heterogeneous cross-linking and structural disorder, which precludes precise modulation of the elastic energy landscape (Fig. 1a).[13] To transcend these topological limitations, we implemented a synergistic spring-entanglement design. This strategy modularizes the mechanical response by integrating an ideal entropy-driven elastic network with topologically entangled domains, allowing the independent regulation of elastic storage and strain accommodation without resorting to irreversible energy-dissipating mechanisms, such as sacrificial bond rupture.

The construction of the synergistic network was initiated by the synthesis of a highly uniform covalent scaffold using thiol-ene click chemistry.[14] The precise reaction between thiol groups (from pentaerythritol tetrakis(3-mercaptopropionate) (PETMP) and 2,2'-(ethylenedioxy)diethanethiol (EDDET)) and acrylate groups (from poly(ethylene glycol) diacrylate (PEGDA)) creates a homogeneous covalent backbone characterized by spring-like athermal elasticity (the elastomer is called a spring-like elastomer (SE), Fig. 1b). The high regioselectivity and efficiency of click chemistry minimize network defects and dangling chains, effectively resolving the stochastic topology issue typical of traditional elastomers synthesized by free radical polymerization. The incorporation of ionic liquids (1-ethyl-3-methylimidazolium bis(trifluoromethylsulfonyl)imide (EMIM TFSI) and 1-ethyl-3-methylImidazolium dicyamide (EMIM DCA)) yields a spring-like ionic elastomer (SIE) that preserves the structural integrity and uniformity of the covalent scaffold. To introduce extensibility while maintaining high elasticity, we strategically integrate ultra-high-molecular-weight polymer chains (polyvinylpyrrolidone (PVP) and poly(propylene glycol)-block-poly(ethylene glycol)-block-poly(propylene glycol) (PPG-PEG-PPG)) to form topological entanglements.[15] PVP mainly provides robust long-chain topological constraints and ionic-liquid affinity, while PPG-PEG-PPG regulates interfacial compatibility, local chain mobility, and nanoscale phase organization.[16,17] Their combination forms topological entanglement domains that delocalize the stress without introducing substantial viscous dissipation (Fig. 1c).

Notably, the click reaction proceeded efficiently under ambient conditions even without a catalyst (Note S1 in ESI). This robust reactivity enables the fabrication of S-SEIE *via* simple co-extrusion and mixing of the two precursor solutions, bypassing the need for conventional energy-intensive triggers such as ultraviolet irradiation or thermal curing (Fig. 1d). The thiol-ene click reaction was monitored using Fourier transform infrared (FTIR) spectroscopy. Before the reaction, PEGDA showed the characteristic absorption of the acrylate C=C bond at approximately 1635 cm^{-1} (Fig. S1 in ESI). After gelation, the characteristic C=C absorption largely disappeared, indicating the consumption of the acrylate groups during the click reaction. This result confirmed that the thiol groups reacted with the acrylate groups and formed a covalently crosslinked elastomer network. Consequently, S-SEIE possesses exceptional processability, allowing it to be readily cast into complex geometries (Fig. S2 in ESI). The resulting elastomer was macroscopically homogeneous, semi-transparent, and exhibited exceptional conformability, as demonstrated by its ability to withstand arbitrary bending and twisting (Fig. 1e).

Rheological analysis of the polymer precursors confirmed a marked transition into the entangled regime, supported by a significant increase in viscosity from 16.9 mPa·s to 46.5 mPa·s (Fig. S3 in ESI). The macroscopic semi-transparency of S-SEIE suggests the formation of nanoscale spatial partitions. Atomic force microscopy (AFM) phase imaging revealed a well-defined nanophase separation consisting of bright (stiff) domains and dark (soft) regions, which correspond to the entangled domains and elastic scaffold, respectively (Fig. 1f). This morphology is further corroborated by small-angle X-ray scattering (SAXS) measurements, showing a domain spacing of approximately 14 nm, which is consistent with the phase-resolved AFM observations (Fig. 1g, Fig. S4 and Note S2 in ESI).[18] This spatial distribution ensures that the load-bearing covalent springs and stress-distributing entanglements occupy distinct topological environments, preventing dissipative modes from interfering with the primary elastic recovery. In contrast, the control samples (SE and SIE), which lacked long-chain polymers, exhibited significantly more homogeneous structures (Fig. S5 in ESI). This contrast confirms that the ob-

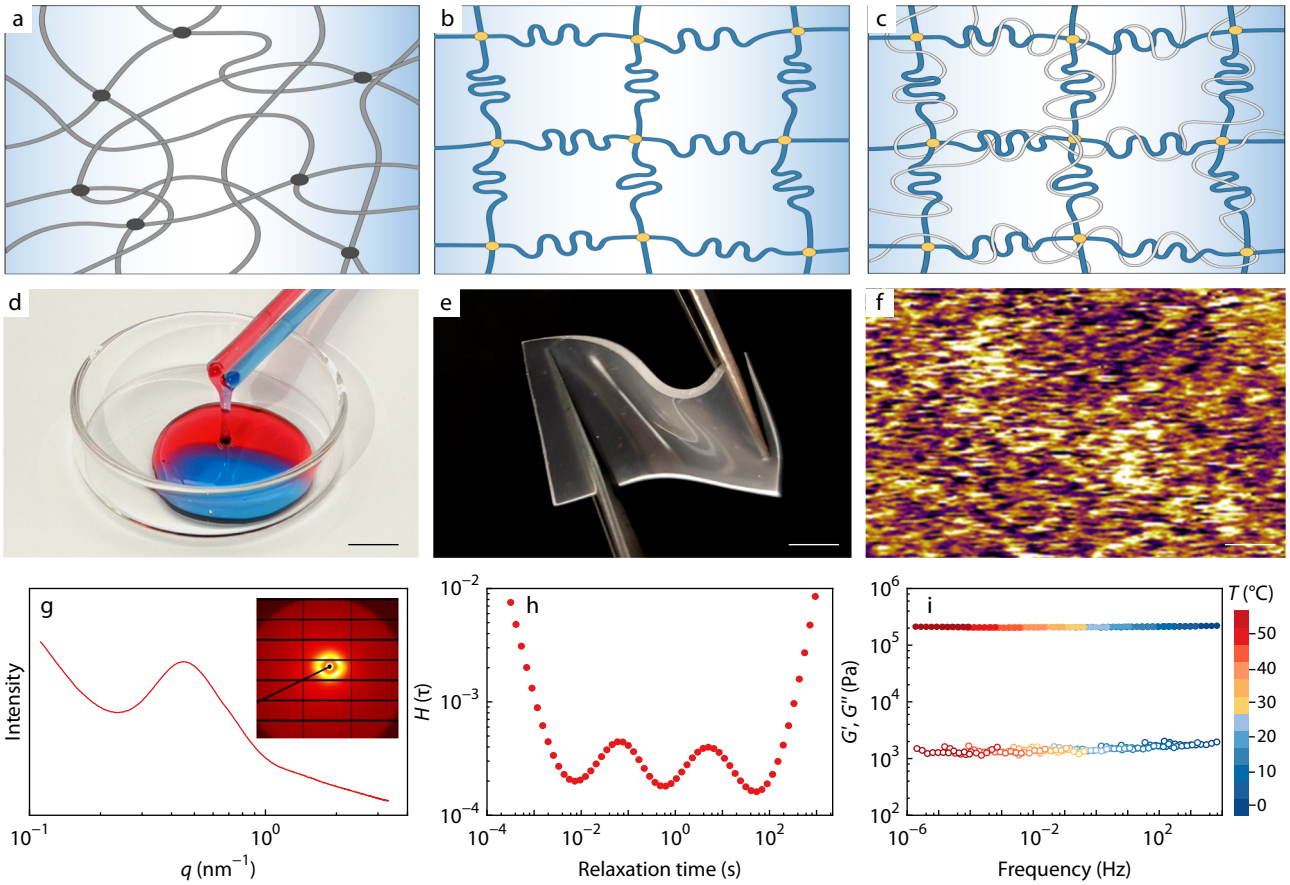

Fig. 1 Topological modulation enables an S-SEIE. (a) Schematic of a conventional polymer network showing random, non-uniform cross-linking due to stochastic polymerization. (b) Schematic of the engineered spring-like covalent network. Efficient thiol-ene click chemistry enables a precisely controlled, homogeneous architecture. (c) Schematic of the final architecture of the S-SEIE. Long-chain polymers create topological entanglement domains that function as non-dissipative stress delocalizers. (d) A photograph showing the facile one-step synthesis of the S-SEIE. Red and blue dyes are added to the two precursor solutions only for visualizing the mixing process and are not included in the actual S-SEIE samples used for characterization. Scale bar: 1 cm. (e) A photograph shows the excellent flexibility and mechanical robustness of the S-SEIE. Scale bar: 1 cm. (f) An AFM phase image revealing well-defined nanophase separation. Bright and dark regions correspond to entangled domains and the soft elastic matrix, respectively. Scale bar: 100 nm. (g) SAXS profile confirms a well-defined nanophase morphology. (h) Relaxation time spectrum. The two discrete relaxation modes correspond to the kinetically differentiated responses of the covalent spring network and the physical entanglements. (i) TTS master curves of the S-SEIE. The storage (G') and loss (G'') moduli across ten orders of frequency demonstrate robust mechanical homeostasis.

served nanophase separation in S-SEIE originates from the entangled PVP and PPG-PEG-PPG chains, validating our topological modulation approach.

This unique architecture translates into a differentiated kinetic landscape of mechanical responses. The relaxation time spectrum derived from rheological measurements exhibited two discrete modes (Fig. 1h). The fast relaxation mode ($\tau_1 \approx$ 0.06 s) originated from the rapid entropic re-equilibration of the uniform covalent scaffold, which served as the source of high elasticity and near-zero hysteresis.[19] Conversely, a slow relaxation mode ($\tau_2 \approx 5.05$ s) corresponds to the cooperative reptation and topological shuffling of entangled long chains.[20] Crucially, these entangled chains act as nondissipative stress distributors. They remain dynamically frozen during rapid elastic recovery to maintain the modulus while becoming active under large-strain loading to prevent stress concentration. The pronounced separation of these two relaxation modes directly evidences the kinetically differentiated response of the network, which underlies the rare combination of high modulus and high toughness.

To validate the mechanical stability afforded by our design, we compared the dynamic behavior of S-SEIE with polydimethylsiloxane (PDMS). Unlike PDMS, which shows frequency-dependent increases in G' and tanδ, S-SEIE maintains a remarkably stable G' and a near-constant, ultra-low tanδ across the entire frequency range (Fig. S6 in ESI). Time-temperature superposition (TTS) master curves further confirmed this stability, with G' remaining nearly independent of frequency across ten orders of magnitude (10^{-6}–10^{4} Hz) (Fig. 1i). The high apparent activation energy (E_a=243 kJ·mol^{-1}) derived from Arrhenius analysis indicates a high barrier to structural rearrangement, confirming the robust mechanical stability of the click chemistry network (Fig. S7 and Note S3 in ESI).[21]

Mechanical Responses of the S-SEIE

To validate the independent dynamics of the synergistic design,

specifically that the introduction of physical entanglements does not compromise the mobility of the elastic matrix, we performed ^{1}H low-field nuclear magnetic resonance (LF-NMR) analysis (Figs. 2a and 2b). The transverse relaxation time (T_2) provides a sensitive probe of local proton dynamics and segmental activity.[22] In SE, the click-chemistry network exhibited a short T_2 value (0.5 ms), reflecting severe topological constraints imposed by dense covalent cross-linking. Remarkably, the click-chemistry network in S-SEIE with physical entanglement exhibits an even higher T_2 value of 1.2 ms. This increase indicates that the introduction of high-molecular-weight polymers does not hinder the activity of the primary elastic network. In addition, S-SEIE exhibits two additional peaks at 21.5 and 200.9 ms, which are assigned to ionic-liquid-rich environments with different degrees of activity. The peak at 21.5 ms corresponds to a more constrained ionic liquid that interacts more strongly with the click-chemistry network, whereas the peak at 200.9 ms arises from a less constrained, more mobile ionic liquid. These strong interactions ensure the effective confinement of the ionic liquids within the network, thereby suppressing their leakage. Spatial partitioning ensures that the entangled domains and elastic matrix occupy distinct regions, where the entanglements contribute to the average dynamics without hindering the entropic freedom of the network. This finding provides evidence that S-SEIE successfully incorporates stress-redistributing pathways while preserving the fast-relaxing and athermal nature of the ideal elastic network.

The macroscopic consequences of the synergistic design were further evaluated through mechanical tensile testing (Fig. 2c and Note S4 in ESI). As predicted by the Lake-Thomas model, both the SE and SIE exhibit brittle failure with fracture strains below 51%, regardless of the modulus (approximately

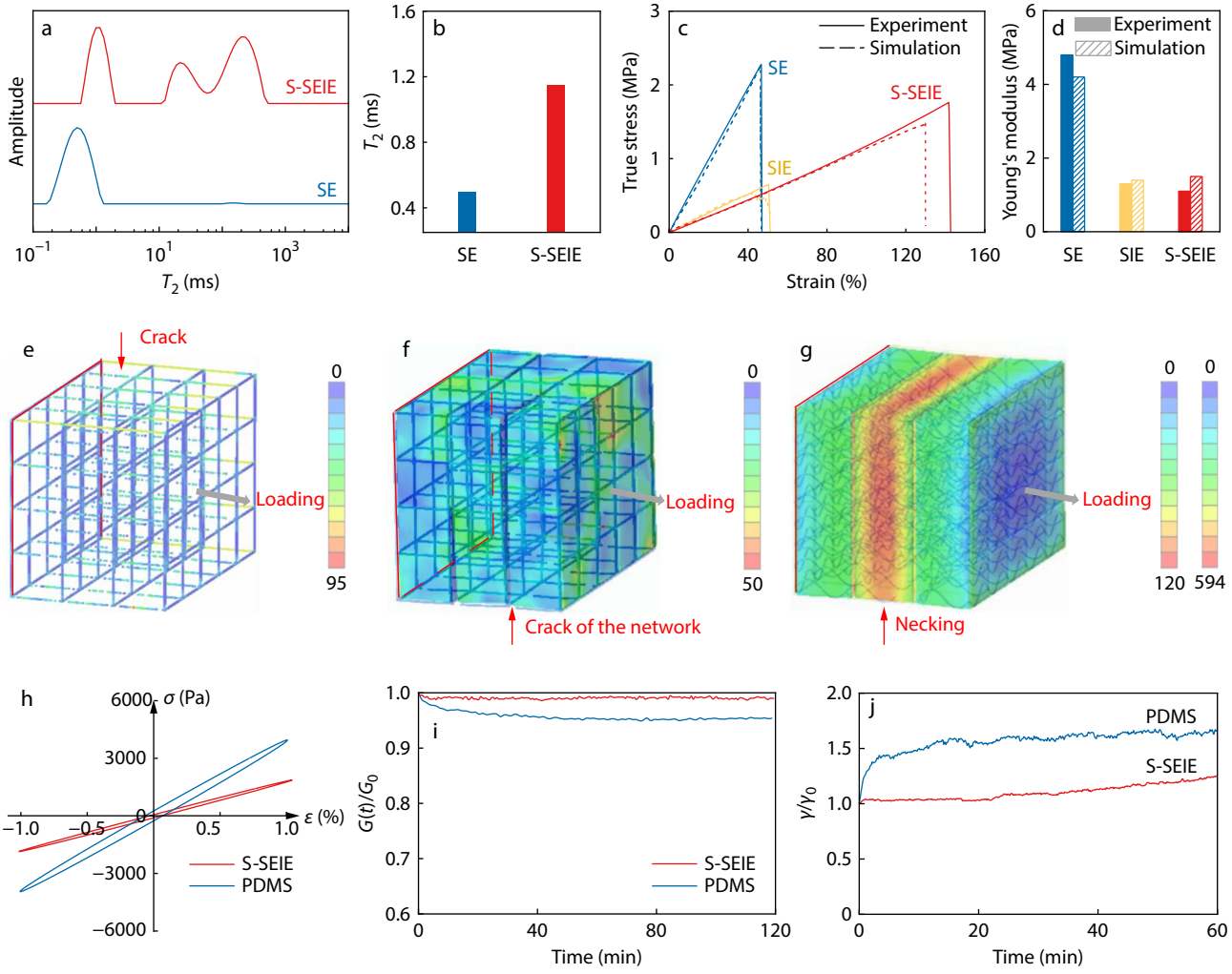

Fig. 2 Experimental and computational validation of topological modulation and mechanical homeostasis in the S-SEIE. (a) The low-field ^{1}H-NMR spectra of SE and S-SEIE; (b) The corresponding T_2 values of SE and S-SEIE; (c) A comparison between experimental measurements and FEA simulations, highlighting the increased stretchability of the S-SEIE without modulus degradation; (d) Statistics of the modulus of the SE, SIE, and S-SEIE, obtained from both experimental measurements and theoretical simulations; (e) FEA stress evolution maps and numerical contour distributions at peak loading for the SE; (f) FEA stress evolution maps and numerical contour distributions at peak loading for the SIE; (g) FEA stress evolution maps and numerical contour distributions at peak loading for the S-SEIE; (h) LAOS tests comparing the S-SEIE and PDMS, illustrating the ultra-low energy dissipation and superior elasticity of the S-SEIE; (i) Stress relaxation profiles at 1% shear strain, showcasing the near-ideal elastic retention of the S-SEIE; (j) The creep curves of the PDMS and the S-SEIE at a shear stress of 100 Pa.

https://doi.org/10.1007/s10118-026-3780-9

4.8 and 1.3 MPa). Their premature failure is ascribed to the lack of stress-redistribution pathways, leading to stress localization at topological defects. In contrast, S-SEIE maintains a high Young's modulus (>1 MPa) while extending the fracture strain to 142%. It should be noted that S-SEIE contains approximately 50 wt% ionic liquids, and its formulation-based polymer/network fraction is comparable to that of the SIE control sample. Therefore, this enhanced stretchability originates from the nanophase-separated entangled domains rather than a simple increase in the polymer content, as these domains provide a distributed pathway for stress energy without resorting to sacrificial bond rupture. Accordingly, S-SEIE is selected as the optimized architecture because it achieves a balanced combination of MPa-level modulus, enhanced stretchability, and near-zero hysteresis.

Notably, the ionic elastomer exhibited exceptional linearity in its true stress-strain curve up to 142% strain, providing a stable mechanical foundation for quantitative ionotronic sensing. This performance was further corroborated by finite element analysis (FEA), where the simulated curves closely matched the experimental results (Fig. 2d). Furthermore, fracture energy measurements show a toughening effect for S-SEIE (350 J·m^{-2}) compared to SIE (250 J·m^{-2}) (Fig. S8 and Note S5 in ESI). This increase indicates that the topological entanglements function as non-dissipative stress delocalisers, effectively enhancing the toughness without introducing heavy hysteresis.

To visualize this reinforcement mechanism at the mesoscopic level, FEA was employed to map the stress evolution across the three architectures (Figs. 2e–2g). In the SE and SIE models, the absence of stress-redistributing components led to rapid elastic energy accumulation at topological defects, triggering immediate stress localization and brittle rupture (Figs. 2e and 2f). In contrast, in the S-SEIE architecture, the physical entanglement domains functioned as highly effective stress delocalizers (Fig. 2g). Under loading, these domains facilitated controlled segmental sliding and stretching, diffusing the stress intensity across the entire material volume. This multiscale redistribution of stress explains the nearly threefold increase in stretchability, confirming that the synergy of the elastic scaffold and stress-distributing domains is the key to bypassing the classical stiffness-stretchability trade-off.

The elasticity of S-SEIE was then compared to PDMS, which is a benchmark for ideal elasticity, through a large-amplitude oscillatory shear (LAOS) experiment (Fig. 2h and Note S6 in ESI).[23] Under a periodic sinusoidal alternating strain (1%), the dissipated energy (ΔW) for PDMS and S-SEIE are 4.1×10^{-7} and 1.3×10^{-7} J, respectively. The lower ΔW of S-SEIE definitively confirms its exceptional elasticity, validating that the homogeneous click-chemistry network functions as an ideal athermal molecular spring.

The robust mechanical stability afforded by this elastic network was further demonstrated through a comparative stress-relaxation study (Fig. 2i). Over time, the relaxation modulus $G(t)$ gradually decreased and reached a plateau, reflecting the time-dependent viscoelastic behavior.[24] However, the $G(t)/G_0$ value for S-SEIE remained remarkably high at 0.99, even outperforming the PDMS control (0.95). This indicates that the long-range topological constraints of the covalent click network effectively locked the transient entanglements over extended periods, preventing macroscale structural flow despite the presence of slower relaxation modes. To ensure a reliable sensor performance, the material must be fundamentally creep-free and leakage-free. Under a continued load for 1 h, S-SEIE exhibited a small strain change, whereas the PDMS control showed a large strain increase of up to 1.5 times its initial value (Fig. 2j). Simultaneously, S-SEIE demonstrated excellent long-term stability against ionic liquid leakage. This combination of structural and electrochemical stability provides the ultimate barrier against functional signal drift, establishing S-SEIE as a prime candidate for high-precision and ultra-low-drift ionotronic sensing.

Excellent Elasticity and Fatigue Resistance of the S-SEIE

The hierarchical spring-entanglement design endows S-SEIE with robust mechanical stability, which is definitively confirmed by cyclic tensile and compressive tests across various strains and rates. When subjected to cyclic tensile deformation over a broad strain range of 20% to 100%, S-SEIE consistently demonstrated a nearly hysteresis-free mechanical response (Fig. 3a). Notably, the mechanical properties exhibited striking rate insensitivity. Even within a broad strain rate range of 0.08–0.42 s^{-1}, the material retains an almost constant Young's modulus (1.0–1.1 MPa) and an ideal linear stress-strain relationship (Fig. 3b and Fig. S9 in ESI). This linear relationship establishes a mechanical basis for high-accuracy and high-fidelity sensing over a broad strain range.

To quantify the elastic efficiency, we evaluated the hysteresis during the cyclic tensile tests, which is defined as the ratio of the energy dissipated to the energy input during loading. Even at a high strain rate of 0.42 s^{-1}, the hysteresis of S-SEIE remains remarkably low at <0.51% (Note S7 in ESI).[25] This ultra-low value indicates minimal irreversible energy dissipation during dynamic deformation. This ideal elastic behavior originates from the synergistic effect of the architecture. The click-derived covalent scaffold provides instantaneous entropic recoil, whereas topological entanglements mediate local stress redistribution without inducing the viscous drag typically associated with sacrificial bonds. During continuous compression up to 60% strain, the residual strain after the stress release remained below 0.46% (Fig. 3c). Moreover, under cyclic compression at varying strain rates (8.3×10^{-3} to 3.5×10^{-2} s^{-1}), the stress-strain curves of the first and tenth cycles overlapped almost perfectly (Fig. 3d, Figs. S10 and S11 in ESI).

Moreover, we compared S-SEIE with state-of-the-art elastic gels and elastomers (Fig. 3e and Table S1 in ESI). Conventionally, low hysteresis has been achieved primarily by reducing the crosslinking density, which minimizes energy dissipation during deformation. However, despite the hysteresis being as low as 0.13%–13.5%, this strategy inevitably compromises network stiffness, resulting in a relatively low modulus of only 15–90 kPa.[26–30] To overcome this limitation, highly entangled networks have been explored as an alternative route to improve the modulus without substantially increasing hysteresis.[31–37] Nevertheless, enhanced entanglement is associated with a higher density of polymer chains. The trade-off

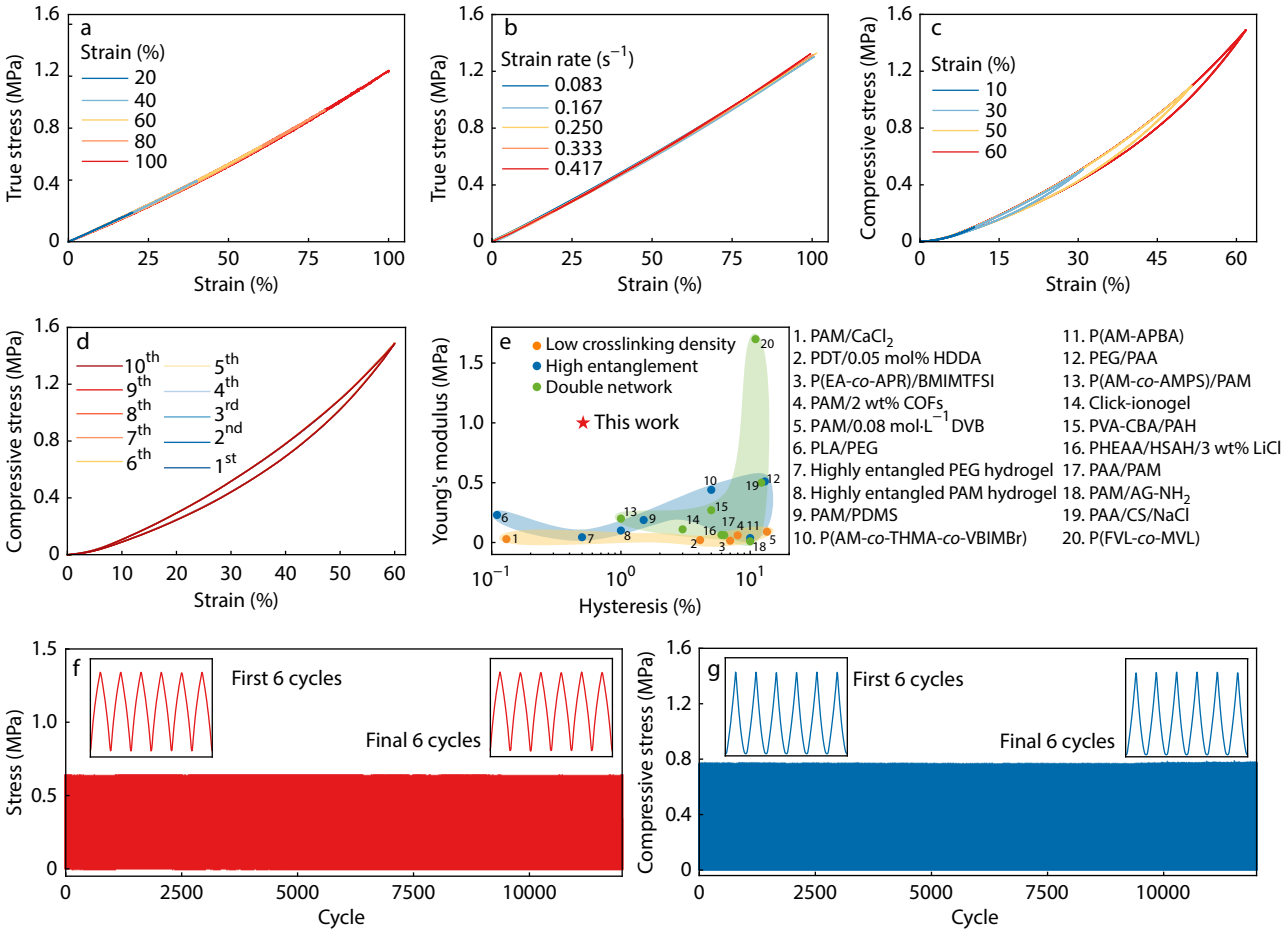

Fig. 3 Exceptional elasticity, rate-insensitive mechanical homeostasis, and long-term fatigue resistance of the S-SEIE. (a) Cyclic tensile true stress–strain curves of the S-SEIE at varying strains (20% to 100%), demonstrating a nearly hysteresis-free elastic response; (b) Cyclic tensile curves at 100% strain under varying strain rates, highlighting the rate-insensitive nature of the entropy-driven covalent scaffold; (c) Cyclic compressive stress–strain curves at incremental strains, showing minimal irreversible energy dissipation and extremely low residual strain; (d) Ten continuous compressive cycles at 60% strain and a strain rate of 8.3×10^{-3} s^{-1}, confirming rapid and fully reversible structural recovery; (e) The comparison of the Young's modulus and hysteresis of the S-SEIE with state-of-the-art elastic gels and elastomers. The S-SEIE uniquely breaches the classical stiffness-elasticity ceiling. (f) Long-term cyclic tensile fatigue evaluation over 1.2×10^4 cycles at 100% strain, exhibiting impeccable mechanical stability with negligible stress attenuation; (g) Long-term cyclic compressive fatigue evaluation over 1.2×10^4 cycles at 40% strain, underscoring the non-destructive load-bearing capability of the hierarchical topological network.

between the modulus and high elasticity was only partially alleviated, and the resulting modulus remained limited to 37–440 kPa. On the other hand, double-network architectures can dramatically increase the modulus to 1×10^{-2}–1.7 MPa.[14,38–44] However, the incorporation of sacrificial networks introduces additional energy dissipation, typically leading to hysteresis values above 1%. In contrast, S-SEIE maintains an ultra-low hysteresis (<0.51%) even at 100% strain while simultaneously achieving a Young's modulus of >1 MPa, which is an order of magnitude higher than that of typical low-hysteresis gels or elastomers. This effectively breaches the classical stiffness-elasticity ceiling and establishes a benchmark for high-performance soft elastomers.

The structural robustness of S-SEIE is further underscored by its impressive fatigue resistance during long-term cyclic measurements. In cyclic tensile tests up to 100% strain for 1.2×10^4 cycles, S-SEIE maintained high mechanical stability, exhibiting a peak stress variation of <1% (Fig. 3f). This remarkable durability is evident under cyclic compression. After 1.2×10^4 compression cycles at 40% strain, S-SEIE exhibited a negligible residual strain (<0.7%) and minimal stress attenuation (<5%) (Fig. 3g). Such outstanding fatigue resistance arises from the non-destructive nature of topological reinforcement. Because the entangled structure accommodates strain without breaking covalent bonds, the material avoids the accumulation of microdamage that plagues dissipative double-network elastomers. Consequently, S-SEIE successfully translates its mechanical homeostasis into long-term durability, ensuring highly stable and reliable performance for demanding human-machine interfaces.

Sensitive and Ultra-low-drift Sensing Performance of the S-SEIE

The presence of an ideal entropy-driven elastic network endows S-SEIE with ultralow mechanical hysteresis, making it a promising candidate for high-fidelity flexible sensors. The material exhibits a high electrical conductivity of 0.4 $S\cdot m^{-1}$ at room

temperature (Fig. S12 and Note S8 in ESI). As ion migration and interfacial charge accumulation dictate the capacitive response, this intrinsic ionic conductivity provides an essential electrochemical foundation for device fabrication.[45]

Leveraging its exceptional elasticity, we constructed a sandwich-structured capacitive sensor using S-SEIE as a deformable active layer. Surface microstructures with a thickness of 500 μm were fabricated on a 2 mm-thick S-SEIE film, which was then sandwiched between two carbon cloth electrodes (Fig. S13 in ESI). In this configuration, S-SEIE functions as an ion conductor and carbon cloth as an electronic conductor. Upon contact, mobile ions accumulate at the interface, forming a nanometer-thick electric double layer (EDL) that functions as a giant capacitor.[46] Because the total capacitance is highly dependent on the interfacial contact area, this microstructured design yields a highly sensitive sensor that exhibits three distinct pressure-response regimes (Fig. 4a). In the low-pressure regime (<0.1 MPa), the sensor achieves a remarkable sensitivity of 0.19 kPa^{-1} (Note S9 in ESI). This high sensitivity arises from the initial deformation of the surface microstructures, which rapidly maximizes the effective EDL contact area between the electrode and S-SEIE. In the intermediate-pressure range (0.1–0.4 MPa), the sensitivity decreases to 0.08 kPa^{-1} as the microstructures progressively collapse. Ultimately, in the high-pressure regime (0.4–0.62 MPa), the sensitivity declines to 0.04 kPa^{-1}.

Crucially, the high elasticity of S-SEIE minimizes energy dissipation, ensuring rapid and synchronous establishment and relaxation of the EDL interface. When a sudden pressure of 0.007 MPa was applied and maintained for 5 s, the sensor exhibited perfectly symmetrical response and recovery times of only 200 ms (Fig. 4b). During the hold phase, the signal displays absolute stability without observable drift, which is a macroscopic consequence of the leakage-free and creep-free mechanical stability of S-SEIE. Furthermore, the sensor delivered accurate and highly repeatable capacitive responses under cyclic compression across various stress levels (0.024–0.62 MPa) and compression rates (0.0051–0.025 s^{-1}), underscoring the rate-insensitive and almost drift-free nature of the microstructured S-SEIE (Fig. 4c and Fig. S14 in ESI). Remarkably, even after 10^4 compression cycles at 0.14 MPa, the sensor exhibited ultra-low signal drift (0.95%) and no observable microstructural damage, confirming unparalleled compressive sensing stability (Fig. 4d and Fig. S15 in ESI). These results collectively indicate that the entropy-driven recoil of the click network ensures highly reversible structural recovery, translating directly into high-fidelity and ultralow-drift sensing.

In addition to robust capacitive sensing under compression, S-SEIE is a highly reliable resistive strain sensor under tensile deformation, demonstrating the versatility of the synergistic network across distinct mechanical modes. The strain sensitivity, evaluated *via* the gauge factor (GF), revealed a near-ideal linear correlation between the relative resistance change ($\Delta R/R_0$) and the applied tensile strain (Fig. 4e).[47] As the strain increased from 0% to 100%, $\Delta R/R_0$ increased linearly to 224%, corresponding to a constant GF of approximately 2.24. This broad-range linearity fundamentally originates from the linear true stress–strain response of the underlying

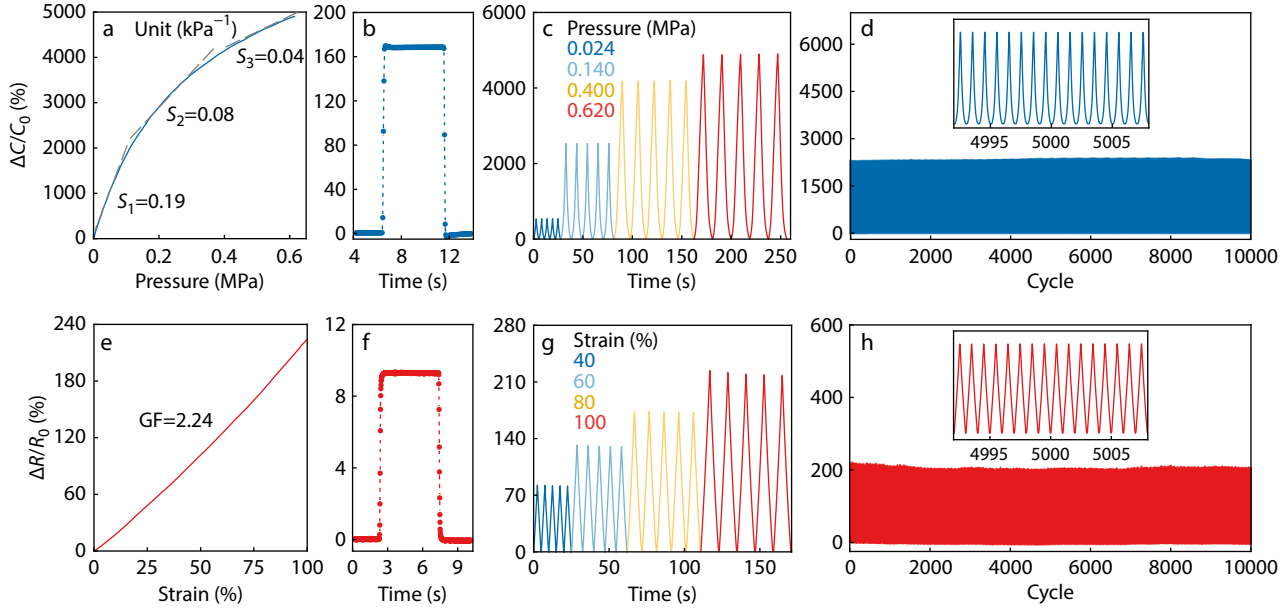

Fig. 4 Sensitive, ultra-low-drift, and multimodal electromechanical sensing performance of the S-SEIE. (a) Relative capacitance change of the microstructured S-SEIE sensor as a function of compressive pressure, exhibiting three distinct sensitivity regimes due to interfacial contact area variation; (b) Rapid, symmetrical response and recovery times (200 ms) under a step compression of 7 kPa for 5 s, demonstrating the non-dissipative elastic response; (c) Dynamic capacitive responses to cyclic compression at escalating applied pressures, showcasing high sensitivity and signal reproducibility; (d) Long-term cyclic compressive stability test for 10^4 cycles at 0.14 MPa, highlighting the structural fatigue resistance and ultra-low baseline drift; (e) Relative resistance change of the S-SEIE versus tensile strain, revealing a broad-range, highly linear electromechanical correlation (Gauge factor of about 2.24); (f) Ultrafast resistive response and recovery times under a 5% step tensile strain for 5 s; (g) Reversible and highly repeatable resistive responses under continuous cyclic tensile loading at incremental strains; (h) Long-term cyclic tensile durability test for 10^4 cycles at 100% strain, confirming the robust mechanical stability and signal fidelity of the synergistic network under extreme deformation.

https://doi.org/10.1007/s10118-026-3780-9

S-SEIE. This direct synchronized mapping between macroscopic strain and electrical resistance eliminates the need for complex calibration algorithms and establishes a reliable mechanical basis for high-accuracy quantitative analysis.

This superior tensile elasticity was further validated by its ultrafast temporal response. Upon applying and holding a 5% step strain for 5 s, the sensor exhibited rapid, symmetric response, and recovery times of 200 ms (which is close to and limited by the sampling frequency of the instrument) (Fig. 4f). Because this rapid recovery is driven by instantaneous entropic chain recoil rather than slow dynamic bond reformation, it is entirely nondissipative. Consequently, the $\Delta R/R_0$ output of the sensor remained exceptionally stable and rate-insensitive across a broad dynamic range (0.083–0.333 s^{-1}) (Fig. S16 in ESI). Most critically, the tensile sensor maintained excellent durability and signal fidelity. Under continuous cyclic testing at escalating strains (40%, 60%, 80%, and 100%), the sensor generated highly reproducible waveforms without baseline drift (Fig. 4g). Even after enduring 10^4 cycles at 100% strain, the sensor delivered an unwavering signal output with near-zero attenuation (Fig. 4h). This outstanding signal reproducibility was the ultimate validation of the synergistic spring-entanglement design. An ideal covalent scaffold guarantees rapid, fully reversible structural recovery, maintaining intact ionic transport pathways, and stable interfacial contact. Such unprecedented signal repeatability and ultra-low-drift performance make S-SEIE a transformative material platform for advanced soft robotics and high-precision bio-integrated devices.

High-fidelity Pulse Monitoring and Vibro-acoustic Sensing

Benefiting from the stable and highly sensitive response of the microstructured S-SEIE, we demonstrated its utility in detecting ultra-weak physiological and environmental signals. First, we noninvasively monitored subtle pulse fluctuations at the human wrist to evaluate real-time cardiovascular health. When a miniaturized S-SEIE capacitive sensor was securely attached to the wrist, it clearly captured the three critical characteristic peaks of the arterial pulse wave: systolic peak (P_1), reflected wave peak (P_2), and diastolic peak (P_3) (Figs. 5a and 5b). The resolution of these features is paramount for assessing cardiovascular conditions (Note S10 in ESI).[48] The ability to sharply resolve these high-frequency, transient features stems directly from the rapid and hysteresis-free electromechanical response of the covalent click network. Because the sensor's recovery speed significantly surpasses the pulse rate, it achieves a high temporal accuracy without signal smearing or baseline drift.

Furthermore, owing to the exceptional sensing reliability and structural durability of S-SEIE, the sensor stably monitors the pulse activity over extended periods. As shown in Fig. 5(c), each pulse beat over a continuous recording was flawlessly resolved into three characteristic peaks, demonstrating the capability to capture complex cardiovascular dynamics with high resolution (Movie S1 in ESI). Statistical analysis over three consecutive days revealed an average heart rate of approximately 83 beats per minute, falling within the normal physiological range (Fig. S17 in ESI). Remarkably, despite the minute capacitance variations ($\Delta C/C_0$) induced by the weak pulse pressure, the sensor delivered a highly sensitive and strictly stable detection. This unwavering signal stability provides the ultimate validation of the nondestructive, creep-free mechanical stability afforded by our hierarchical topological design. Consequently, S-SEIE enables the reliable quantitative extraction of cardiovascular metrics, such as the P_2/P_1 amplitude ratio, which is a clinically relevant parameter for arterial stiffness.

Beyond physiological monitoring, the microstructured S-SEIE functioned as an exceptional vibro-acoustic transducer, exhibiting high-fidelity acoustic perception (Movie S2 in ESI). As shown in Fig. 5(d), an acoustic monitoring setup was assembled to evaluate the response of the sensor to airborne sound waves. The sensor demonstrated acute sensitivity to

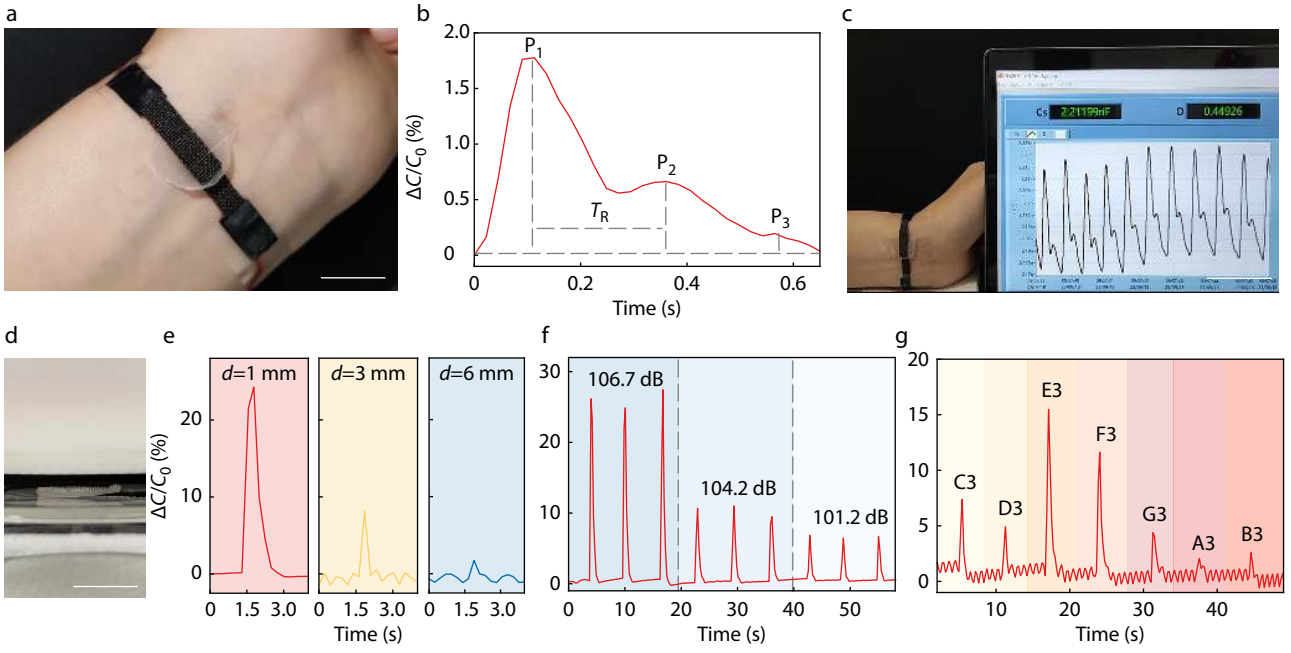

https://doi.org/10.1007/s10118-026-3780-9

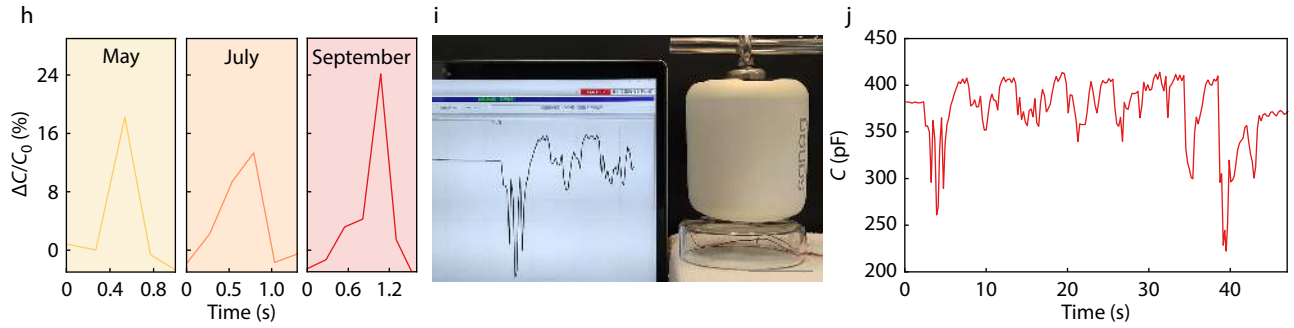

Fig. 5 High-fidelity physiological pulse monitoring and vibro-acoustic sensing enabled by the microstructured S-SEIE. (a) A photograph showing the conformal attachment of the microstructured S-SEIE sensor to the human wrist for pulse monitoring. Scale bar: 1 cm. (b) High-resolution relative capacitance profile of a single arterial pulse wave, precisely resolving the systolic (P_1), reflected (P_2), and diastolic (P_3) characteristic peaks without signal smearing. (c) A photograph of the experimental setup displaying the real-time acquisition of the pulse signal, demonstrating the stable monitoring of complex cardiovascular dynamics. Scale bar: 4 cm. (d) A photograph of the vibro-acoustic testing setup, with the S-SEIE positioned 3 mm away from a loudspeaker to capture airborne sound waves. Scale bar: 1 cm. (e) Distance-dependent capacitance response of the microstructured S-SEIE, highlighting the extreme sensitivity to air-pressure fluctuations. (f) Sound-intensity-dependent capacitance response (at a fixed 1 mm distance) of the microstructured S-SEIE. (g) High-fidelity acoustic discrimination of sequentially played piano keys across varying musical scales (C3 to B3). (h) Precise phonological recognition resolving the distinct syllabic patterns of monosyllabic ("May"), disyllabic ("July"), and trisyllabic ("September") words. (i) A photograph of the experimental setup for acoustic monitoring measurements during music playback. Scale bar: 2 cm. (j) The corresponding real-time capacitance variations recorded during music playback.

variations in the acoustic pressure. Among the different octave notes A (A1, A2, and A3), A2 induced the strongest vibrational response and was therefore selected for detailed measurements (Fig. S18 in ESI). We observed a precise, positive correlation between the capacitance change and acoustic intensity, which can be modulated by either decreasing the source distance (6 to 1 mm) or increasing the decibel level (101.2 to 106.7 dB). This confirms that the surface microstructures effectively captured minute air pressure fluctuations (Figs. 5e, 5f, and Fig. S19 in ESI).

Crucially, the entropy-driven elastic network ensures ultralow energy dissipation and ultrafast segmental recoil under dynamic acoustic deformation, granting the sensor exceptional signal fidelity and real-time responsiveness. These attributes enable a sophisticated phonological recognition. The sensor not only discriminates between distinct piano keys (C3 to B3) but also precisely resolves complex syllabic patterns in human speech (Fig. 5g and Fig. S20 in ESI). For instance, the sensor accurately identified the number of syllables in a spoken word using the corresponding number of distinct capacitance peaks (Fig. 5h). The monosyllabic word "May" produced a single sharp peak, whereas the trisyllabic word "September" generated a primary peak flanked by two distinct shoulder peaks. Additionally, the pronunciation duration recorded by the sensor (1.04 s) aligned almost perfectly with the actual audio duration analyzed by the software (1.13 s) (Fig. S21 and Table S2 in ESI). This negligible temporal lag confirms that S-SEIE underwent zero viscous retardation, even under high-frequency acoustic loading.

The device demonstrated a high signal-to-noise ratio (SNR), effectively isolating meaningful vocal signals from background interference. During audio playback, the sensor remained unresponsive to continuous background music, yet synchronously and exclusively captured the sharp capacitance peaks corresponding to human vocals (Figs. 5i, 5j, and Movie S3 in ESI). Collectively, this extraordinary capability to capture, discriminate, and temporally resolve complex acoustic information highlights that the hierarchical spring-entanglement design completely circumvents the traditional viscoelastic limitations. By translating topological mechanical stability into impeccable sensory fidelity, S-SEIE paves the way for next-generation wearable auditory interfaces and precision biointegrated electronics.

CONCLUSIONS

In summary, we resolved the intrinsic trade-off between segmental relaxation dynamics and cohesive interaction density in ion-conductive elastomers through a synergistic spring-entanglement network. By synergistically integrating a spring-like covalent network with topological entanglement domains, the resulting elastomer achieved an exceptional combination of Young's modulus (approximately 1 MPa), ultra-low hysteresis (<0.51%), and reliable extensibility (142%). We demonstrated that these superior mechanical properties are a physical prerequisite for high-fidelity ionotronic sensing. By incorporating surface microstructures, the elastomer enables the precise sensing of cardiovascular pulse waves and vibro-acoustic signals with ultralow baseline drift. The ability to maintain mechanical stability for over 10^4 cycles ensures long-term functional integrity. This study establishes a versatile methodological framework for designing durable and high-performance soft materials for advanced bio-integrated electronics.

Conflict of Interests

The authors declare no interest conflict.

Electronic Supplementary Information

Electronic supplementary information (ESI) is available free of charge in the online version of this article at http://doi.org/10.1007/s10118-026-3780-9.

Data Availability Statement

The related data of this study is data that should not be shared, and can be obtained from the author for reasonable reasons. The author's contact information: wupeiyi@dhu.edu.cn.

ACKNOWLEDGMENTS

This work was financially supported by the National Natural Science Foundation of China (Nos. 22305033 and 52573019 received by Z.Y.L., No. 52433003 received by P.Y.W.), and the Fundamental Research Funds for the Central Universities (No. 2232024A-05 received by Z.Y.L.).

REFERENCES

1 Keplinger, C.; Sun, J.-Y.; Foo, C. C.; Rothemund, P.; Whitesides, G. M.; Suo, Z. Stretchable, transparent, ionic Conductors. *Science* **2013**, *341*, 984–987.
2 Zhou, N.; Zhang, L.; Cui, T.; Wu, P.; Lei, Z. Design and applications of conductive polymers in wearable electrophysiological sensing. *Sci. China Technol. Sci.* **2025**, *68*, 2200204.
3 Lee, Y.; Lim, S.; Song, W. J.; Lee, S.; Yoon, S. J.; Park, J.-M.; Lee, M.-G.; Park, Y.-L.; Sun, J.-Y. Triboresistive touch sensing: grid-free touch-point recognition based on monolayered ionic power generators. *Adv. Mater.* **2022**, *34*, 2108586.
4 Zhou, X.; Yin, J.-F.; Chen, C.; Chi, Y.; Chen, J.; Liu-Fu, W.; Yang, J.; Long, S.; Tang, L.; Yao, X.; Yin, P. Hierarchical supramolecular aggregation of molecular nanoparticles for granular materials with ultra high-speed impact-resistance. *Adv. Sci.* **2024**, *11*, 2405285.
5 Liu, X.; Wu, J.; Qiao, K.; Liu, G.; Wang, Z.; Lu, T.; Suo, Z.; Hu, J. Topoarchitected polymer networks expand the space of material properties. *Nat. Commun.* **2022**, *13*, 1622.
6 Lake, G. J.; Thomas, A. G. The strength of highly elastic materials. *Proc. A* **1967**, *300*, 108–119.
7 Liu, J.; Yang, C.; Yin, T.; Wang, Z.; Qu, S.; Suo, Z. Polyacrylamide hydrogels. II. elastic dissipater. *J. Mech. Phys. Solids* **2019**, *133*, 103737.
8 Nonoyama, T.; Gong, J. P. Tough double network hydrogel and its biomedical applications. *Annu. Rev. Chem. Biomol. Eng.* **2021**, *12*, 393–410.
9 Zheng, Y.; Gong, J. P. Viscous solvent effect on fracture of predamaged double-network gels examined by pre-notch and post-notch crack tests. *J. Mech. Phys. Solids* **2025**, *194*, 105926.
10 Li, X.; You, X.; Wang, X.; Kang, J.; Zhang, H. J. Advanced lignin-based hydrogels with superior stiffness, toughness, and sensing capabilities. *Adv. Funct. Mater.* **2025**, *35*, 2415744.
11 Seiffert, S. Origin of nanostructural inhomogeneity in polymer-network gels. *Polym. Chem.* **2017**, *8*, 4472–4487.
12 Bao, B.; Shi, C.; Zeng, Q.; Chen, T.; Xiao, C.; Jiang, L.; Liu, T.; Lyu, J.;

Graphical Abstract

Synergistic Spring-entanglement Network Design of High-modulus and Low-hysteresis Ionic Elastomers for High-fidelity Sensing

Ting Cui, Jing-Ming Cai, Cun-Yi Li, Zhou-Yue Lei, and Pei-Yi Wu

Donghua University, China; Southeast University, China; University of Technology Sydney, Australia; Aalto University, Finland

A synergistic spring-entanglement network combines the click-derived covalent network with topological stress delocalization, yielding a stretchable, low-hysteresis ion-conductive elastomer with rapid recovery and stable drift-free performance over 10^4 cycles.

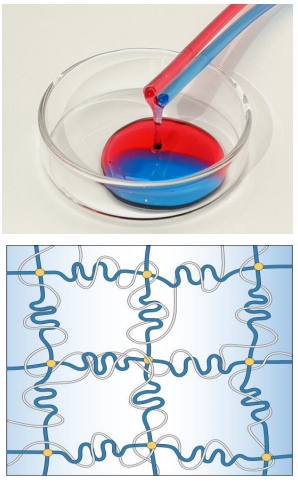

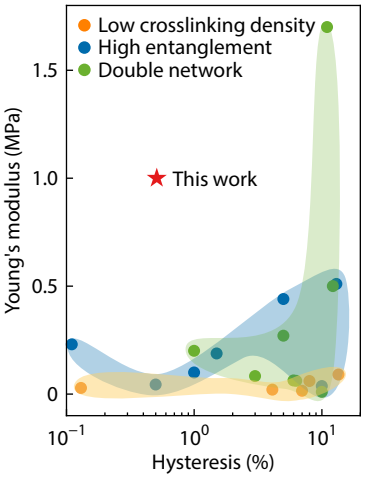

Chinese J. Polym. Sci., 2026 *https://doi.org/10.1007/s10118-026-3780-9*

Wang, W.; Zhu, L.; Lin, Q. Photocoupling of propagating radicals during polymerization realizes universal network strengthening. *Nat. Synth.* **2025**, *4*, 1522–1533.
13 Shibayama, M. Spatial inhomogeneity and dynamic fluctuations of polymer gels. *Macromol. Chem. Phys.* **1998**, *199*, 1–30.
14 Ren, Y.; Guo, J.; Liu, Z.; Sun, Z.; Wu, Y.; Liu, L.; Yan, F. Ionic liquid–based click-ionogels. *Sci. Adv.* **2019**, *5*, eaax0648.
15 Liu, L.; Li, J.; Wang, S.; Xiang, Y.; Lu, T.; Gao, Y. Tough and anti-swelling naturally derived adhesives by long-chain toughening and electrostatic attraction. *Polymer* **2025**, *336*, 128870.
16 Huang, Z.; Xu, L.; Liu, P.; Peng, J. Transparent, mechanically robust, conductive, self-healable, and recyclable ionogels for flexible strain sensors and electroluminescent devices. *RSC Adv.* **2024**, *14*, 28234–28243.
17 Jorge, A. M. S.; Silva, G. M. C.; Coutinho, J. A. P.; Pereira, J. F. B. Unravelling the molecular interactions behind the formation of PEG/PPG aqueous two-phase systems. *Phys. Chem. Chem. Phys.* **2024**, *26*, 7308–7317.
18 Jiang, Y.; Tang, N.; Wang, X.; Pei, D.; Zhang, H.; Li, M.-H.; Hu, J. Mechanically robust eutectogels enabled by precisely engineered crystalline domains. *Nat. Commun.* **2025**, *16*, 7417.
19 Zhang, L.; Liu, S.; Wang, Z.; Lei, Z.; Wu, P. An enthalpy-entropy compensated ionogel with a broadband viscoelastic plateau for non-invasive and high-fidelity neurointerfaces. *Adv. Mater.* **2026**, *38*, e21208.
20 Zhou, N.; Cui, T.; Lei, Z.; Wu, P. Bioinspired learning and memory in ionogels through fast response and slow relaxation dynamics of ions. *Nat. Commun.* **2025**, *16*, 4573.
21 Zhu, W.; Wu, B.; Lei, Z.; Wu, P. Piezoionic elastomers by phase and interface engineering for high-performance energy-harvesting ionotronics. *Adv. Mater.* **2024**, *36*, 2313127.
22 Liu, Y.; Zhang, J.; Wu, P. Near-frictionless long-distance water transport in trees enabled by hierarchically helical molecular pumps. *CCS Chem.* **2025**, *7*, 484–492.
23 Wang, H.; Wang, H.; Chen, D.; Tian, X.; Yang, J.; Liu, W. Solvent polarity-induced ultrahigh strength supramolecular polyzwitterionic organogels with impact-stiffening, damping, and anti-freezing properties. *Small* **2025**, *21*, 2501737.
24 Yuan, Z.; Cao, Z.; Wang, H.; Wu, H.; Zheng, J.; Zhang, R.; Wu, J. Tough hydrogels enabled by transient entanglements. *Nat. Commun*. **2026**, *17*, 4145.
25 Zhao, L. J.; Tang, N.; Wang, X. T.; Li, M. H.; Hu, J. Conductive polyaniline hydrogel featuring high toughness and low hysteresis. *Chinese J. Polym. Sci.* **2025**, *43*, 581–587.
26 Wang, J.; Tang, F.; Yao, C.; Li, L. Low hysteresis hydrogel induced by spatial confinement. *Adv. Funct. Mater.* **2023**, *33*, 2214935.
27 Xue, Q.; He, X.; Lei, J.; Hong, W.; Yang, C. Synergizing network topology and solvent compatibility for gels with hyperelasticity and omniadhesion. *Sci. Adv.* **2026**, *12*, eaec7718.
28 Du, R.; Bao, T.; Zhu, T.; Zhang, J.; Huang, X.; Jin, Q.; Xin, M.; Pan, L.; Zhang, Q.; Jia, X. A low-hysteresis and highly stretchable ionogel enabled by well dispersed slidable cross-linker for rapid human-machine interaction. *Adv. Funct. Mater.* **2023**, *33*, 2212888.
29 Li, W.; Wang, X.; Liu, Z.; Zou, X.; Shen, Z.; Liu, D.; Li, L.; Guo, Y.; Yan, F. Nanoconfined polymerization limits crack propagation in hysteresis-free gels. *Nat. Mater.* **2024**, *23*, 131–138.
30 Tan, S.; Wang, C.; Yang, B.; Luo, J.; Wu, Y. Unbreakable hydrogels with self-recoverable 10200% stretchability. *Adv. Mater.* **2022**, *34*, 2206904.
31 Hou, X.; Huang, B.; Zhou, L.; Liu, S.; Kong, J.; He, C. An amphiphilic entangled network design toward ultratough hydrogels. *Adv. Mater.* **2023**, *35*, 2301532.
32 Nian, G.; Kim, J.; Bao, X.; Suo, Z. Making highly elastic and tough hydrogels from doughs. *Adv. Mater.* **2022**, *34*, 2206577.
33 Kim, J.; Zhang, G.; Shi, M.; Suo, Z. Fracture, fatigue, and friction of polymers in which entanglements greatly outnumber cross-links. *Science* **2021**, *374*, 212–216.
34 Wang, Z.; Yang, F.; Liu, X.; Han, X.; Li, X.; Huyan, C.; Liu, D.; Chen, F. Hydrogen bonds-pinned entanglement blunting the interfacial crack of hydrogel–elastomer hybrids. *Adv. Mater.* **2024**, *36*, 2313177.
35 Wang, W.; Guo, P.; Liu, X.; Chen, M.; Li, J.; Hu, Z.; Li, G.; Chang, Q.; Shi, K.; Wang, X.; Lei, K. Fully polymeric conductive hydrogels with low hysteresis and high toughness as multi-responsive and self-powered wearable sensors. *Adv. Funct. Mater.* **2024**, *34*, 2316346.
36 Xu, K.; Shen, K.; Yu, J.; Yang, Y.; Wei, Y.; Lin, P.; Zhang, Q.; Xiao, C.; Zhang, Y.; Cheng, Y. Ultradurable noncovalent cross-linked hydrogels with low hysteresis and robust elasticity for flexible electronics. *Chem. Mater.* **2022**, *34*, 3311–3322.
37 Bao, X.; Chen, Z.; Nian, G.; Tan, M. W. M.; Ahn, C. H.; Kutsovsky, Y.; Suo, Z. Unusually long polymers crosslinked by domains of physical bonds. *Nat. Commun.* **2025**, *16*, 4749.
38 Zhu, R.; Zhu, D.; Zheng, Z.; Wang, X. Tough double network hydrogels with rapid self-reinforcement and low hysteresis based on highly entangled networks. *Nat. Commun.* **2024**, *15*, 1344.
39 Li, T.; Li, X.; Yang, J.; Sun, H.; Sun, J. Healable ionic conductors with extremely low-hysteresis and high mechanical strength enabled by hydrophobic domain-locked reversible interactions. *Adv. Mater.* **2023**, *35*, 2307990.
40 Sun, Y.; Cheng, Y.; Shi, L.; Sun, J.; Chen, S.; Wang, R. Dual ion regulated eutectogels with high elasticity and adhesive strength for accurate strain sensors. *Adv. Funct. Mater.* **2024**, *34*, 2401808.
41 Zhang, S.; Ren, D.; Zhao, Q.; Peng, M.; Wang, X.; Zhang, Z.; Liu, W.; Huang, F. Observation of topological hydrogen-bonding domains in physical hydrogel for excellent self-healing and elasticity. *Nat. Commun.* **2025**, *16*, 2371.
42 Zhao, X.; Xu, J.; Zhang, J.; Guo, M.; Wu, Z.; Li, Y.; Xu, C.; Yin, H.; Wang, X. Fluorescent double network ionogels with fast self-healability and high resilience for reliable human motion detection. *Mater. Horiz.* **2023**, *10*, 646–656.
43 Li, X. L.; Shang, W. D.; Xu, T. Q. Super-tough and resilient recyclable polyester elastomers enabled by dynamic cross-linking. *Macromolecules* **2026**, *59*, 2292–2301.
44 Chen, M.; Qin, W.; Wang, Y.; Zhai, H.; Gu, C.; Zhao, X.; Bi, Y.; Xu, Y.; Ming, Z.; Li, S.; Hu, S.; Zhang, X.; Ma, X.; Yin, S. Dynamic Na+ bridges: a 3D printing strategy for hydrogels with high strength, low hysteresis, strong adhesion, and self-healing. *Adv. Funct. Mater.* **2026**, *36*, e24993.
45 Zhan, H.; Lei, Z.; Wu, P. Colossal piezoionic effect from hierarchical asymmetries in soft ionotronics. *Adv. Mater*. **2026**, *38*, e73067.
46 He, Y.; Cheng, Y.; Yang, C.; Guo, C. F. Creep-free polyelectrolyte elastomer for drift-free iontronic sensing. *Nat. Mater.* **2024**, *23*, 1107–1114.
47 Du, H. Y.; Zhang, J.; Xu, Q.; Cao, Y. C.; Jia, H.; Li, Y. Anti-swelling zwitterionic gels with high stretchability, conductivity for wireless underwater strain sensing. *Chinese J. Polym. Sci.* **2026**, *44*, 792–802.
48 Wu, J.; Fan, X.; Liu, X.; Ji, X.; Shi, X.; Wu, W.; Yue, Z.; Liang, J. Highly sensitive temperature–pressure bimodal aerogel with stimulus discriminability for human physiological monitoring. *Nano Lett.* **2022**, *22*, 4459–4467.

https://doi.org/10.1007/s10118-026-3780-9